# 3T TROMBONE COIL FOR MR SMALL ANIMAL IMAGING

# An Undergraduate Research Scholars Thesis by AALIYAH FISHER

Submitted to the Undergraduate Research office at Texas A&M University in partial fulfillment of requirements for the designation as an

#### UNDERGRADUATE RESEARCH SCHOLAR

Approved by Faculty Research Advisor:		Dr. Mary McDougall
	May 2025	
Major:		Biomedical Engineering

Copyright © 2025. Aaliyah Fisher.

#### RESEARCH COMPLIANCE CERTIFICATION

Research activities involving the use of human subjects, vertebrate animals, and/or biohazards must be reviewed and approved by the appropriate Texas A&M University regulatory research committee (i.e., IRB, IACUC, IBC) before the activity can commence. This requirement applies to activities conducted at Texas A&M and to activities conducted at non-Texas A&M facilities or institutions. In both cases, students are responsible for working with the relevant Texas A&M research compliance program to ensure and document that all Texas A&M compliance obligations are met before the study begins.

I, Aaliyah Fisher, certify that all research compliance requirements related to this

Undergraduate Research Scholars thesis have been addressed with my Faculty Research Advisor
prior to the collection of any data used in this final thesis submission.

This project did not require approval from the Texas A&M University Research Compliance & Biosafety office.

# TABLE OF CONTENTS

			Page
AF	BSTRA	CT	1
DE	EDICA	ΓΙΟΝ	3
AC	CKNOV	WLEDGEMENTS	4
NO	OMENO	CLATURE	5
1.	INTRO	ODUCTION	6
	1.1 1.2 1.3	MRI Basics	9
2.	METH	HODS	16
	2.1 2.2 2.3	Mathematical Design SolidWorks Design Physical Coil Construction Details	17
3.	RESU	ILTS	22
	3.1 3.2 3.3	Log Mag Plots	24
4.	CONC	CLUSION	29
	4.1 4.2	Q – Factor and Q – Ratio Analysis	
RE	EFERE	NCES	31
AF	PPEND	IX: A - LOGARITHMIC MAGNITUDE PLOTS	34
ΑF	PEND	IX: B – SMITH CHARTS	40

#### **ABSTRACT**

3T Trombone Coil for MR Small Animal Imaging

Aaliyah Fisher Department of Biomedical Engineering Texas A&M University

Faculty Research Advisor: Dr. Mary McDougall Department of Biomedical Engineering Texas A&M University

The theoretical design of a radio frequency (RF) birdcage coil for magnetic resonance imaging (MRI) often deviates from its anticipated performance. Theoretical equations used to describe birdcage coil parameters are for ideal capacitances and inductances, neglecting parasitism, specimen loading, and other real-world influences. When RF coils are loaded with specimens, achieving the desired resonant frequency requires iterative adjustments of the coils tuning capacitance. Tuning capacitors for a high-pass birdcage coil are located between each rung along both end rings, requiring at least 24 capacitors for a 12-rung birdcage coil to be swapped out for each iteration. In addition to these parameter limitations, clinical RF coils are limited to a single resonant frequency, restricting their versatility in multi-nuclei imaging applications. These limitations create a need for a clinical probe that is easily adjustable and tunable across a range of resonant frequencies, enabling seamless acquisition of data for various resonating nuclei without the need to exchange probes. This works seeks to address this gap by designing a trombone birdcage coil specifically for small animal studies, such as those involving rats and mice. Unlike the traditional birdcage design, a trombone RF coil allows for frequency

adjustment by varying the inductance, facilitating more efficient tuning to multiple frequencies. The quality factor (Q factor) and s-parameters will be evaluated through benchtop testing, with future assessment taking place on a clinical scanner to measure signal-to-noise ratio (SNR). The trombone coil will then be utilized for *in-vivo* imaging. This innovative approach aims to improve the versatility and functionality of RF coils, streamlining experimental workflows and enhancing the quality of multi-nuclei imaging.

# **DEDICATION**

This Thesis is dedicated to my incredible parents, whose unwavering support has been the foundation of my academic journey and personal growth. Your encouragement, love, and belief in me have shaped the person I strive to become. I am eternally grateful.

#### **ACKNOWLEDGEMENTS**

#### **Contributors**

I would like to thank my faculty advisor, Dr. McDougall, for her guidance and support throughout this project. I would also like to thank Ph.D. Candidates, Jacob Degitz and Donald Bowen for lending their advice, skills, and expertise over the course of this research.

Thanks also to my friends, colleagues, and the department faculty for making my time at Texas A&M University a great experience.

The trombone coil components, and benchtop tests were analyzed/used for "3T Trombone Coil for Small Animal MR Imaging" were provided by Dr. McDougall, Jacob Degitz, Donald Bowen, and Rose Gigliotti. The analyses depicted in "3T Trombone Coil for Small Animal MR Imaging" were conducted in part by Dr. McDougall's NMR RF Laboratory within the Biomedical Department at Texas A&M University and this data is unpublished.

All other work conducted for the thesis was completed by the student independently.

# **Funding Sources**

This research was not funded by any specific grant but was paid for through the discretionary funds of the NMR RF Laboratory.

# **NOMENCLATURE**

MRI Magnetic Resonance Imaging

NMR Nuclear Magnetic Resonance

MR Magnetic Resonance

RF Radio Frequency

CT Computed Tomography

*B*<sub>0</sub> Static Magnetic field (aligning with nuclei spins)

 $B_1$  Radio Frequency Magnetic field (transmitted by RF coils perpendicular to  $B_0$ ).

T Tesla's (magnitude of magnetic field)

Hz Hertz (measure of frequency)

ROI Region Of Interest

SNR Signal-to-Noise Ratio

Q-Factor Quality Factor

#### 1. INTRODUCTION

#### 1.1 MRI Basics

#### 1.1.1 How MRI Works

A magnetic resonance imaging (MRI) scanner is a type of noninvasive diagnostic imaging device that provides detailed cross-sectional and 3D images of the body. This is performed through the generation of both a static magnetic field and radio frequency waves that interact with the "spin" of atomic nuclei commonly found in fluids within the body such as hydrogen [1]. MRI is mainly used in cases where soft tissues of the body, such as brain, muscle, and internal organs, are being imaged. MRI differs from other imaging techniques, such as computed tomography (CT) and x-ray, since it does not use ionizing radiation but rather radiofrequency pulses. Because of this characteristic, it is the safer option when it comes to repeated imaging as it does not carry the same risk of DNA damage and mutations due to ionizing radiation [2].

#### 1.1.2 Molecular Principles

Before exploring the components of an MRI scanner, it is important to understand the underlying science of MR imaging. For most clinical applications, hydrogen nuclei (protons) are the focus of the scanner, as they are abundant within the body and give off a small signal that accumulatively creates a strong enough signal to be detected by the MRI system. It is important to note that all nuclei express a magnetic moment due to the circulation of protons and neutrons within the nucleus. The magnetic moment of a nuclei makes it tiny dipole that can be manipulated by external magnetic fields. MRI technology takes advantage of these properties by applying a static magnetic field ( $B_0$ ) to these nuclei causing them to experience a torque (due to

their magnetic moments), which makes them "precess" like a spinning top — this is called Larmor precession [3]. Equation 1 models how torque is applied to the nuclei:

$$\tau = m \times B_0 \tag{1}$$

Where  $\tau$  is the torque on the nuclei, m is the magnetic moment of the nuclei, and  $B_0$  is the static magnetic field. This phenomenon is also depicted in Figure 1:

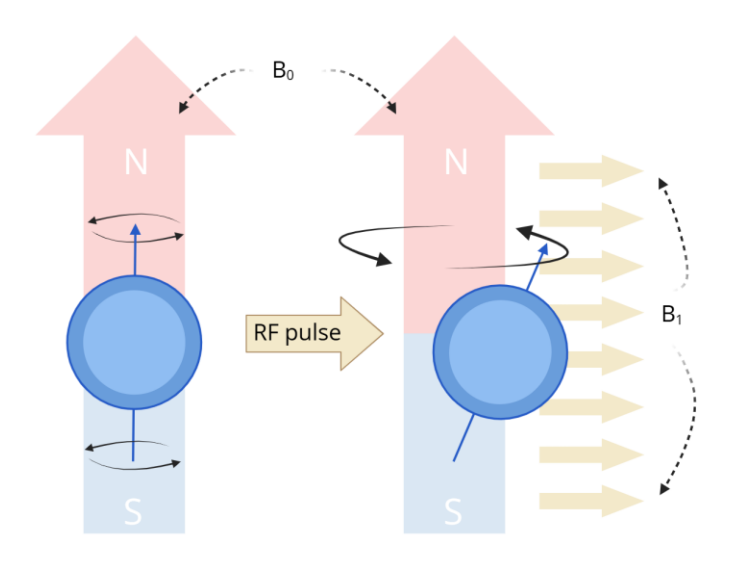


Figure 1: How an atomic nucleus interacts with an external magnetic field

However, only certain nuclei, known as NMR-active nuclei, can be detected in MRI. These nuclei must have an odd number of protons and/or neutrons, which result in a net magnetic moment and allow them to align with the  $B_0$  field as discussed above [4]. There are special cases however, where there can be an even number of nucleons, such is the case with Deuterium ( $^2H$ ) which is occasionally used to tag cancer cells for imaging, among other things [5]. Some of the most regularly imaged/studied NMR-active nuclei are hydrogen-1, sodium-23, and phosphorous-31 [4]. In a normal environment with no external magnetic field, the spin and direction of the atom's axis is random; but when a magnetic field is introduced, torque applied to

the magnetic moments of the nuclei force them to become parallel or antiparallel (parallel in but when the axis is pointed in the opposite direction) with the field. In other words, when a patient is initially placed in an MRI scanner, the NMR active nucleons within the patient's body align with the  $B_0$  field.

When the protons align with this external magnetic influence, the  $B_0$  field, they also begin to spin in phase with the magnetic field. This type of spin that the particle exudes is defined as precession [1], [4]. The precession speed of all NMR active atoms is affected by the strength of the  $B_0$  field and the specific gyromagnetic ratio which is a constant term specific to the nucleon in question [3], [4]. The quantification of this phenomena is called the Larmor equation (can be seen in Equation 2); coined in the late 19th century by Joseph Larmor, an Irish mathematical physicist [3].

$$\omega_0 = \gamma B_0 \tag{2}$$

Where  $\omega_0$  is the Larmor frequency (or precession frequency) in MHz,  $\gamma$  is the gyromagnetic ratio in MHz/T, and  $B_0$  is the external magnetic field in T [3].

This concept is essential to MRI medicine because it helps determine the specific radiofrequency (RF) pulse needed to achieve resonance with NMR-active nuclei. The RF pulse used to excite nuclei, generate a time-varying magnetic field known as the  $B_1$  field, which is applied orthogonally to the  $B_0$  field. Since the  $B_1$  field is applied orthogonally, it temporarily tips the net magnetization of the resonant nuclei out of its original alignment with the  $B_0$  field. Since the  $B_1$  field is applied orthogonally, it temporarily tips the particles net magnetization out of its original alignment with the  $B_0$  field. It is important to note that excitation by the  $B_1$  field is successful because the  $B_1$  field is released at Larmor frequency, allowing for efficient energy absorption by the nuclei. When the RF pulse is turned off, the excited nuclei return to their

original alignment with B<sub>0</sub> through relaxation processes (T<sub>1</sub> and T<sub>2</sub> relaxation). As they do so, they emit RF signals, which induce an electrical current in the receiver coils of the MRI scanner. The received signal represents a summation of magnetization vectors from different tissue regions, producing complex frequency and phase data [6]. These signals are then amplified, digitized, and processed using Fourier transformation, converting the raw frequency-domain data into either a detailed anatomical image or a frequency spectrum, depending on the imaging technique used [7].

#### 1.2 Components of MRI

The three components critical to MRI functionality are: the main electromagnet, the gradient coils, and the RF coil/s. Together, these components incur electromagnetic properties that are able to be translated into an image that physicians can distinguish the different types of tissues within the body.

#### 1.2.1 The Main Electromagnet

The  $B_0$  field is generated by a large, superconducting electromagnet. As discussed before, this field is responsible for the initial alignment of the molecules within the body with its magnetic force [7]. The  $B_0$  field is generally characterized into 3 categories: low field strengths (<1.5 T), high field strengths (3.0 T to 7T), and ultra-high field strengths which are usually values from 7T and above some even reaching 11.7T [7], [8], [9]. Although Ultra-high field imaging for human subjects is uncommon in a clinical setting, research facilities have begun using 7T and 11.7T scanners [10]. Ultra-high field strengths such as 7T have been experimented with, primarily for neuroimaging and some vascular imaging due to its high contrast and higher resolution. The increased quality in image construction has shown to be advantageous for potentially diagnosing neurological disorders such as Alzheimer's, epilepsy, multiple sclerosis,

and psychological conditions through identification of subtle anatomical, functional, and metabolic data [8]. Other scanners in the research field can reach up to 17.2T although these field strengths are designated to small animal subjects only [10]. In summary, modern research suggests that the higher the B<sub>0</sub> field strength, the more sensitive it is, leading to higher resolution images. However, access to high-field scanners is limited because high-strength magnets are more expensive and require specialized infrastructure, such as active shielding and advanced cooling systems, to maintain the equipment [10].

#### 1.2.2 Gradient Coils

The gradient coils make small linear distortions within the  $B_0$  field, creating x, y, and z, magnetic gradients. In other words, there are three gradient coils that create a mapping system allowing for spatial localization in three dimensions (spatial encoding), locating an image slice within the selected x, y, or z plane, and many other spatial functions that can be performed during the pulse sequence though these are the main ones [4]. The gradient coils are electromagnetic, as with many of the components in the machine, which means they produce magnetic fields as electric current runs through the structures [11].

#### 1.2.3 Radiofrequency Coils

The third major component of the MRI system are RF coils. They act as the excitation and reception units of magnetic resonance signals [12]. Although there is a large RF transmit coil built into clinical MRI systems, external RF coils, sometimes referred to as probes, are often used for signal reception [6]. These specialized MRI RF coils were developed around the 1980s when scientists realized that selectively imaging regions of interests (ROIs) were advantageous [12].

#### 1.3 Types of Radiofrequency (RF) Coils

While clinical RF coils are often designed to only transmit or receive signals, some are capable of functioning as both the transmitter and receiver. Those that can transmit and receive release a radiofrequency pulse (quantified in Hz) that produces the  $B_1$  field that is perpendicular to the main magnetic field  $B_0$ . A coil that has transmittance capabilities must have a highly homogeneous  $B_1$  field, and a receive coil must have a high signal-to-noise ratio (SNR) to receive the signals from the patient or subject [10]. There are two main types of RF coils: surface and volume coils [12]. Each type of coil has its advantages and disadvantages, and as such are used in specific applications.

#### 1.3.1 Surface Coils

The first documented instance of the surface coil was introduced by Dr. G. Suryan, who created the first probe coil to measure fluid flow in NMR back in 1951. His research was done by J.R. Singer, in 1959, to measure and characterize blood flow using MR [13]. Around 1980, several papers were published pertaining to Region of Interest (ROI) which was the driving motivation for Dr. Ackerman when he created a small coil that was placed close to the ROI on the specimen which increased the SNR of the scan [12].

Surface coils are made up of a segment of wire in a circular arrangement which creates an inhomogeneous magnetic field that is strong at the center but dissipates fast as the distance from the face of the coil increase [6], [12]. The size and shape of the wire is shaped specifically to the ROI of the specimen being imaged. Although this coil configuration does not usually transmit an RF pulse itself, it has the ability to image a ROI on large patients when it is placed close to the specimen [6]. Within the specialized region of the surface coil, the SNR is high which makes it highly reliable for receiving signals [12]. Because of the small, generated magnetic field that is

strong within and at the edges of the coil, the sensitivity of these coils is greater than that of a volumetric coil. This is a tradeoff; however, as stated earlier, the further away from the surface of the coil the magnetic field resonates, the weaker the field is. Therefore, the placement of these coils on the ROI is important to maximize the quality of the image [12].

#### 1.3.2 Volume Coils

The second type of RF coils are referred to as volume coils. Volume coils are designed to homogenously stimulate and detect RF signals over an expanded field of view (or Region of Interest, ROI). Moreover, they are essential for high-quality imaging of large anatomical regions of a subject that being the head, torso, or whole-body imaging in clinical studies and an entire in vivo specimen in pre-clinical trials [6], [7], [11]. Volume coils come in a plethora of shapes and sizes. These parameters are contingent on multiple factors such as subject, field strength and the imaging requirements of the study [14]. The common structures that are used most traditional volume coils in clinical and research applications are saddle coils and birdcage coils [6].

The saddle coil, also known as the Golay coil, was one of the original volume coil designs for MRI technology. They are distinctly known by their cylindrical configuration with two conductive loops arranged on opposing sides of the coil. Identical current flows through these two loops via a series connection along the longitudinal elements allowing them to be driven by the same amount of current. Because of their simplistic design, they were essential in the early stages of MRI development [15]. The magnetic field produced can be characterized by Equation 3 [6].

$$B_{y} = \frac{2\mu_{0}I}{\pi d} \frac{l}{\sqrt{l^{2}+d^{2}}} \cos\left(\frac{\theta}{2}\right) \tag{3}$$

Where  $\mu_0$  is the permeability of free space is constant, I is the current, d is the diameter of the coil, l is the finite length of the coil, and  $\theta$  is the subtended angle of the two wires with the same current.

Although they do not produce an ideal homogeneous magnetic field for clinical imaging, they are still widely used as RF coils and gradient coils and when central axis placement of the specimen is required. A traditional saddle coil works best in applications where there is a lower gyromagnetic ratio. Because of this saddle coils are commonly seen in NMR systems for high resolution and high field strength applications [6], [7].

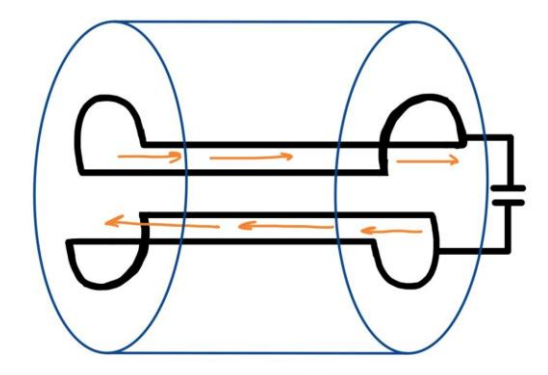


Figure 2: Simple Volumetric Saddle Configuration

As the advancement of MRI technology continued, the need for a more uniform magnetic field produced by RF coil became the focus of RF coil improvement. In the mid 1980's, the birdcage coil configuration was developed to fulfill this need [16].

Birdcage coils were designed off their predecessor, the saddle coil, and have an improved version of NMR coil designs, as they have an increased homogeneous  $B_1$  field, high signal-to-noise ratio (SNR), and are aimed toward higher resonating frequencies [6], [17]. Another advantage of a birdcage configuration is the quadrature transmission. Adding an extra two

circular fields to the preexisting fields from a linearly polarized configuration allows the unwanted, counter-rotating fields to be canceled with each other. This ultimately allows little to wasted power as the other rotating fields (that are not canceled) add together to produce the homogenous  $B_1$  field [18]. The tradeoff for greater field homogeneity at a higher frequency range is its tuning complexity [17].

Due to their high signal-to-noise ratio (SNR), uniform field distribution, and tunable resonance characteristics, the birdcage configuration is widely used for radiofrequency (RF) coils in magnetic resonance imaging (MRI). These coils are typically constructed with evenly spaced conductive elements called "legs" or "rungs" connected by end rings that form a cylindrical "birdcage" structure. Depending on their electrical configuration, birdcage coils are generally categorized into three types: low-pass, band-pass, and high-pass designs [15], [19], [20].

Low-pass birdcage coils incorporate capacitors at the midpoint of each leg, enabling them to resonate at lower frequencies. This configuration is commonly used for body imaging applications where deeper penetration is needed. High-pass designs, in contrast, place capacitors at the junctions between the end rings and the legs, rather than on the legs themselves. These capacitors are symmetrically arranged and are used to achieve resonance at higher frequencies, suitable for applications such as head or extremity imaging [19]. Band-pass configurations, which combine elements of both designs, offer a flexible approach to achieve specific resonance characteristics by distributing capacitors across both the end rings and legs.

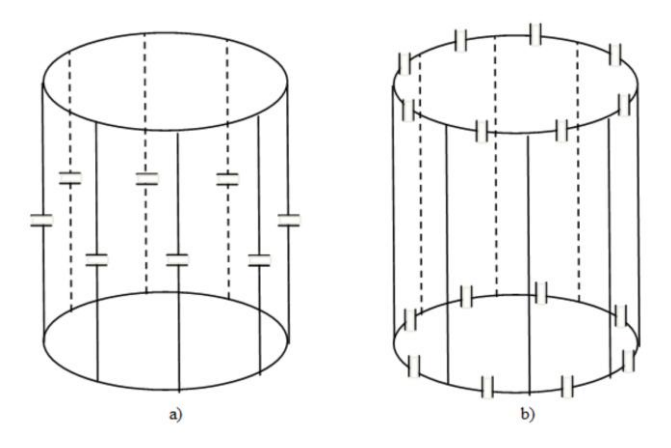


Figure 3: a) Low-Pass Birdcage Configuration; b) High-Pass Birdcage Configuration [15]

While birdcage coils provide excellent homogeneity and tunability, their geometric rigidity and fixed resonance behavior can limit their adaptability in specialized imaging scenarios. This has led to the development of alternative coil designs, such as the **trombone coil**, which introduces dynamic tunability through mechanical adjustment of coil length or capacitance. Trombone coils borrow principles from birdcage architecture but offer greater flexibility by allowing real-time tuning and impedance matching, making them well-suited for multi-nuclear applications or rapidly changing field environments. By integrating variable capacitive elements or sliding conductors, trombone coils can adapt to different loading conditions or anatomical variations without the need for complete circuit redesign [19], [21].

#### 2. METHODS

# 2.1 Mathematical Design

The initial design of the coil was constrained by several factors: tuning capacitance, number of elements, diameter, and length of the coil. Since the coil is specifically aimed at small animals *in vivo* studies, such as mice and rat scans, a coil diameter of 6.5 cm was selected. 12 rungs were included in the design to compromise between field homogeneity and complexity in the smaller coil. Although the standard Larmor frequency for hydrogen at 3.0 T is 127.74 MHz (see Equation 1), the local scanner used for future imaging studies (Siemens Verio) operates at a slightly lower field strength of approximately 2.894 T, resulting in a corresponding target frequency of 123.20 MHz.

To ensure efficient resonance at this high frequency and to minimize wavelength-related effects, the coil length needed to remain below a critical threshold. The wavelength ( $\lambda$ ) of the RF signal was calculated using Equation 4:

$$\lambda = \frac{c}{f\sqrt{\varepsilon_r}}\tag{4}$$

Where, c is the speed of light in a vacuum (3.0 × 10<sup>8</sup> m/s), f is the target frequency (123.20 MHz), and  $\varepsilon_r$  is the relative permittivity, which was set to 1.000536 for air. This gave a wavelength of approximately 244 cm.

To avoid unwanted standing wave effects and ensure proper coil performance, the physical length of the coil was constrained to be less than  $\frac{\lambda}{10}$  or  $\frac{\lambda}{20}$ , as shown in Equation 5:

Length of coil 
$$\leq \frac{\lambda}{n}$$
 where  $(n = 10 \text{ or } 20)$  (5)

Based on this guideline, the coil length had to remain below 24.4 cm  $(\frac{\lambda}{10})$  or ideally below 12.2 cm  $(\frac{\lambda}{20})$ ; therefore, an adjustable range of 12–15 cm was incorporated into the design.

A shield of 20 cm in diameter was used since the increase in shield diameter decreased the magnitude of tuning capacitance. This happens because a larger shield on a relatively small coil will decrease coupling between the shield and the coil [20]. From the parameters discussed above, BirdcageBuilder (an open-source theoretical calculator that uses all the physical parameters of a birdcage coil to predict the necessary tuning capacitance) was used to find the theoretical capacitance needed for a coil length of 13 cm (this is the median length that the coil can be adjusted to) which came out to be about 47 pF [20].

# 2.2 SolidWorks Design

After setting these parameters, all the components of the coil were visualized through a CAD model shown in **Figure 4**.

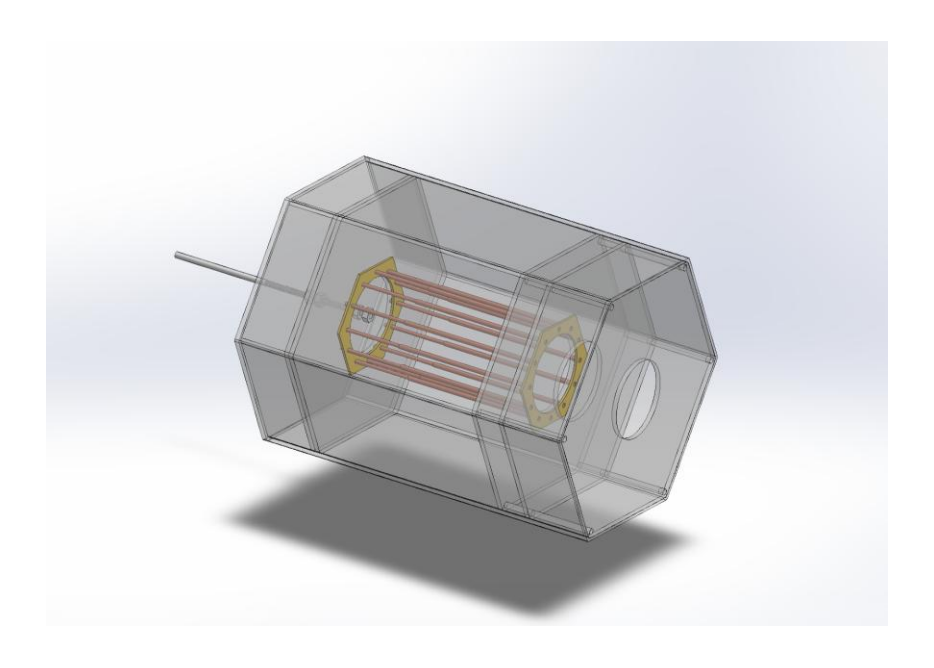


Figure 4: Final SolidWorks Design of Trombone Coil

The CAD design above was constructed via an assembly file on SolidWorks, but each part was saved as an individual file.

# 2.3 Physical Coil Construction Details

After the CAD model was designed, the coil was physically constructed using the materials listed in Table 1.

Table 1: Materials Used to build the Trombone coil.

Material Name	Part of Coil	Number of items	Dimensions
Clear Acrylic	Clear boards between the shield that suspend the RF coil within the shield	6 plates total	Regular Plates: 20 x 20 cm Top Plate: 20.2 cm Center hole diameter: 6.5 cm
	Clear rods used as spacers for the signal line area.	6 rods	Diameter: 1.0 cm
copper-clad FR4 Boards (yellow Fig 4)	The end rings of actual coil components that have rungs and capacitors soldered to it.	2 end rings	Width: 8.5 cm Center hole Diameter: 6.5 cm Holes for copper rungs: 3.97 mm and 3.18 mm
	Trace boards where signal lines and baluns were soldered.	2 boards	Thickness: 1.0 mm Length and Width: 2.7 x 3 cm
Fixed Capacitors  Capacitors soldered to each end ring with a value of 47 pF		24 Capacitors	Thickness: 1.5 mm Length and Width 2.0 x 2.0 mm

Material Name	Part of Coil	Number of items	Dimensions
Copper rungs	Rungs that make up the birdcage coil.	12 large 12 small	Large Rod Diameter: 3.97 mm Small Rod Diameter: 3.18 mm
Nylon rod	Rod that is twisted to adjust the coil length.	1 Rod	Diameter: 1.2 cm
Nylon Nuts	Nuts are used to hold rods in place, and it allows the coil to be incrementally adjusted.	4 Nuts	Width: 1.9 cm Inner Diameter: 1.2 cm
Copper tape, PVC, semi-rigid, kapton tape.	Baluns constructed for signal line impedance matching.	2 Baluns	Diameter: 2.3 cm Length: 2.5 cm
Knowles Voltronics Variable Capacitors	Matching capacitors for signal line impedance matching.	2 Capacitors	N/A

Note: The table above shows all the materials used to create the trombone coil.

The clear plates within the SolidWorks design represent the acrylic boards that were laser cut using the facilities at the ILSQ fabrication laboratory at Texas A&M University. The shield was 3D printed in 4 sections due to the size constraint of the printer, with white PETG filament used to print out the exterior casing seen as clear in Figure 4. The shield was wrapped in copper tape with 2-3 mm gaps between each sheet so that heating of the subject could be avoided

without compromising the integrity of the shield. To prevent coupling of the scanner gradient coils and shield, Kapton tape was placed in between each junction segment.

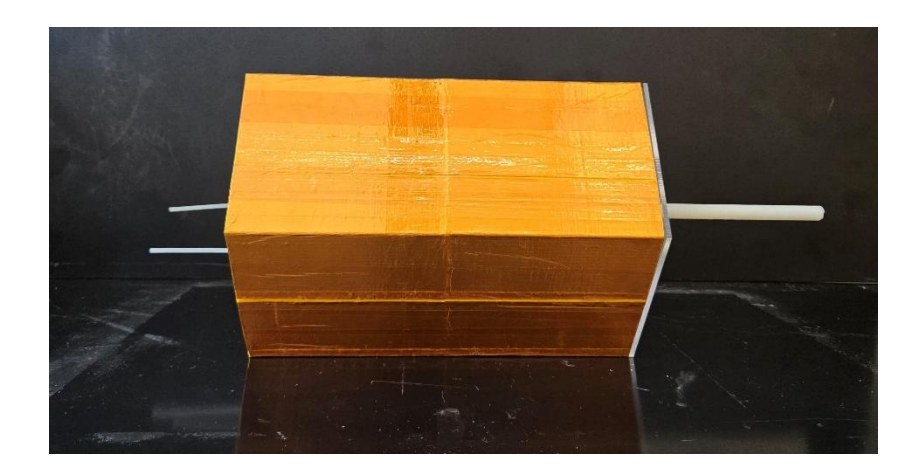


Figure 5: Coil with Final Shield

The trombone coil itself was built using nested copper rods (dimensions listed in Table 2) that were perfectly fitted to where they could easily slide in and out of each other with some slight resistance to create the shrinking and expanding effect. These rods were soldered into two customs made, copper-clad FR4 boards which served as the end rings for the birdcage where the capacitors for the high-pass configuration were implemented.

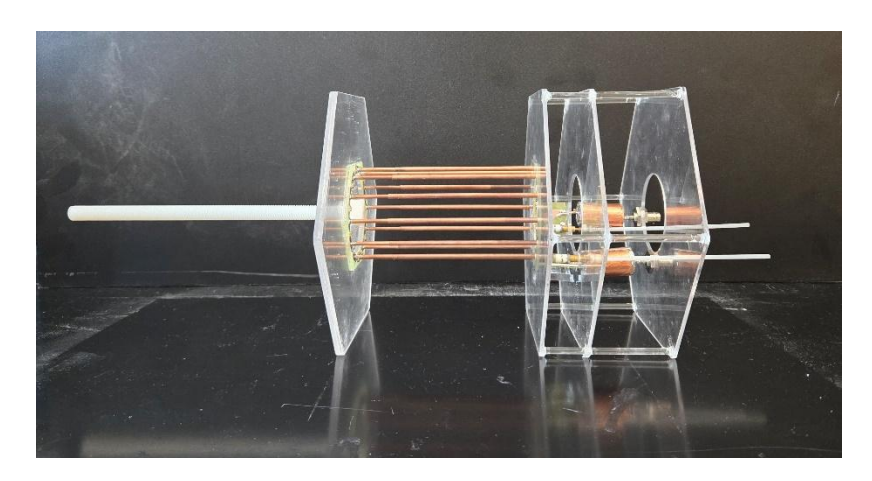


Figure 6: Final Birdcage/Trombone Configuration without the Shield

The nylon rod protruding from the left in Figure 6 was used to adjust the coil and was threaded so that when the coil is nested inside of the shield, the application of an external rotating force was applied to the adjuster rod. The length of the adjuster was arbitrary and could be lengthened for adjustments inside the bore of a scanner for *in vivo* imaging. For now, the size of the adjuster was shorter than normal to allow for easier adjustments during benchtop testing.

# 3. RESULTS

# 3.1 Log Mag Plots

The figures listed in appendix A show the logarithmic output of the coil for ports  $S_{11}$  (yellow) and  $S_{22}$  (blue) individually. This means that readings were taken from each port of the trombone coil separately and were not combined as they should be for a quadrature configuration. Future bench testing will incorporate a quadrature combiner for more accurate evaluation prior to use in the scanner.

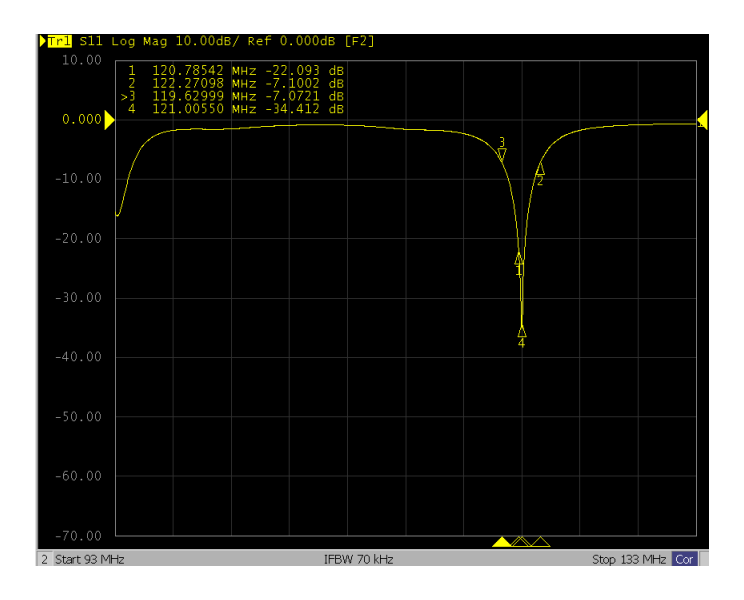


Figure 7: Log Mag of S11 at 13 cm (maximum length) Coil Length Unloaded

Figure 7 is an example of the data collected from the Vector Network Analyzer. The Log Mag scale displays the strength of the coil at the primary resonant frequency in decibels (dB).

Table 2: Resistance Results from Different Coil configurations and the two separate ports  $S_{11}$  and  $S_{22}$ 

	Length of 12 cm	
	Loaded	Unloaded
<b>S</b> <sub>11</sub> (dB)	-15.63	-25.05
Resonant Frequency (MHz)	132.50	130.04
<b>S</b> <sub>22</sub> (dB)	-25.05	-26.80
Resonant Frequency (MHz)	132.51	129.86
Medium	Length (Tuned to 123.20	MHz)
	Loaded	Unloaded
<b>S</b> <sub>11</sub> (dB)	-17.79	-36.13
Resonant Frequency (MHz)	123.48	123.26
<b>S</b> <sub>22</sub> (dB)	-22.84	-24.32
Resonant Frequency (MHz)	123.32	123.09
	Length of 13 cm	
	Loaded	Unloaded
<b>S</b> <sub>11</sub> (dB)	-17.99	-34.41
Resonant Frequency (MHz)	123.48	121.01
<b>S</b> <sub>22</sub> (dB)	-25.49	-41.58
Resonant Frequency (MHz)	123.32	120.67

Note: Table 2 summarizes the data collected from the VNA readings of the Log Mag graphs.

#### 3.2 Smith Charts

The carts in Appendix B illustrate the complex impedance of each coil iteration, plotted on the smith charts. These graphs are crucial for evaluating how effectively each coil is impedance-matched to the 50-ohm standard of the coaxial cables delivering the RF signal to the coil components. As discussed earlier, this matching is achieved using high-range variable capacitors, which are adjusted once the coil is tuned to the desired resonance frequency.

On a Smith chart, the point representing 50 ohms lies at the center, where the real axis intersects with the constant resistance circle at R=1 (normalized). This central location is typically marked as the first reference point. The proximity of each plotted impedance curve to this center point indicates how closely the coil is matched to 50 ohms. A good match minimizes signal reflections and maximizes power transfer to the coil.

It is also important to note that the impedance matching of both RF ports is interdependent. Because of this coupling, the resistance values may deviate slightly from the ideal 50-ohm target, though the goal remains to minimize the mismatch as much as possible.

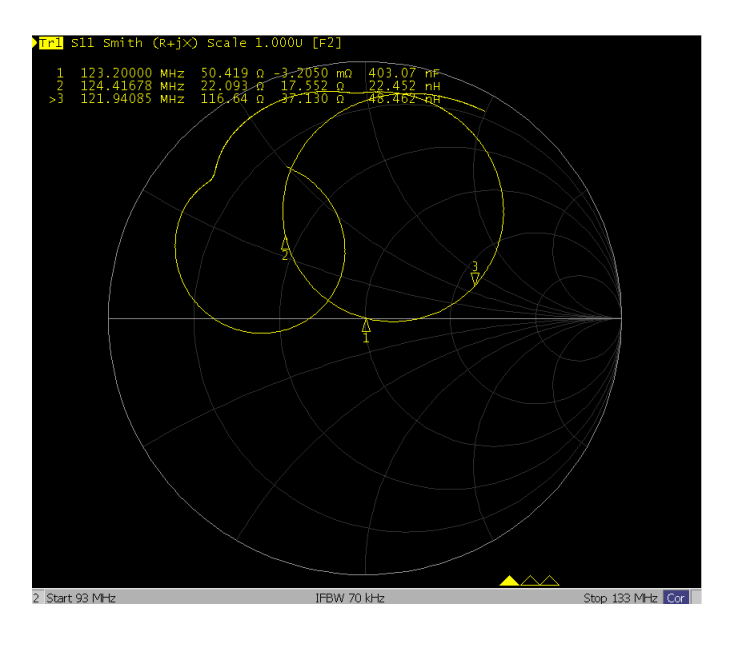


Figure 8:  $S_{11}$  Smith Charts at a medium length (tuned at 123.20 MHz) unloaded.

Figure 8 is an example of a smith chart collected from the VNA. The rest of the images compiled in table 3 are displayed in appendix B.

The table below summarizes the impedance values displayed in each smith chart:

Table 3: Resistance Results from Different Coil configurations and the two separate ports  $S_{11}$  and  $S_{22}$ 

	Length of 12 cm				
	Loaded	Unloaded			
S <sub>11</sub> (ohms)	43.104	45.791			
S <sub>22</sub> (ohms)	53.786	52.262			
Me	Medium Length (Tuned to 123.20 MHz)				
	Loaded	Unloaded			
S <sub>11</sub> (ohms)	50.419	49.425			
S <sub>22</sub> (ohms)	48.532	72.517			
	Length of 13 cm				
	Loaded	Unloaded			
S <sub>11</sub> (ohms)	58.591	53.356			
<b>S</b> <sub>22</sub> (ohms)	46.011	44.842			

Note: Table 2 shows the resistance values taken from each smith chart in the previous figures.

#### 3.3 Q – Factor and Q – Ratio

The table below shows the values for each iteration of coil, loaded and unloaded. The Q – factor is a measurement of how efficient the coil configuration is. It depends on the desired frequency, the inductance of the coil and the resistance of the coil (6).

$$Q = \frac{\omega L}{R} = \frac{f_C}{\Lambda f} \tag{6}$$

Where Q is the Q-factor,  $\omega$  is the resonant frequency, L is the inductance of the coil, and R is the resistance of the coil.

To calculate the Q – factor from the collected data, the center frequency and the bandwidth of the main resonant peak was measured, and was implemented into equation 6, where  $f_c$  is the center frequency of the resonant peak, and  $\Delta f$  is the difference between the 2 peaks measured at -7dB and for smaller peaks.

The Q-ratio (7) is another important value that compares the Q-factor of an unloaded coil to that of a loaded coil. If the Q-ratio is close to 1, then this means the system is coil noise dominant, but if the Q-ratio is greater than 1, then that means that the coil is sample noise dominant, and the coil is performing efficiently.

$$Q_{ratio} = \frac{q_{unloaded}}{q_{loaded}} \tag{7}$$

Where  $Q_{unloaded}$  is the Q – factor of the coil with no sample and  $Q_{loaded}$  is the Q – factor when the coil is loaded with some sort of sample. For benchtop tests, the sample was a bottle of salt water that was placed directly into the center of the coil.

Table 4: Q – Factor Calculations of  $S_{11}$  and  $S_{22}$  with each port Loaded and Unloaded

Q – Factor of Coil Iterations			
Length of 12 cm			
	Loaded	Unloaded	
S <sub>11</sub> (ohms)	56.46	161.99	
S <sub>22</sub> (ohms)	54.93	200.77	
Medi	um Length (tuned to 123.20 I	MHz)	
	Loaded	Unloaded	
S <sub>11</sub> (ohms)	49.68	124.67	
S <sub>22</sub> (ohms)	55.93	205.71	
I	Length of 13 cm	1	
	Loaded	Unloaded	
S <sub>11</sub> (ohms)	45.84	112.10	
S <sub>22</sub> (ohms)	53.64	186.83	

Note: The 3<sup>rd</sup> Table shows the output of the calculations using equation 6 and the frequency values recorded in the figures from the logarithmic magnitude section of results.

Table 5: Q – Ratios from  $S_{11}$  and  $S_{22}$ 

Q – Ratio of Coil Iterations			
	12 cm	Tuned to 123.20 MHz	13 cm
S <sub>11</sub> (ohms)	2.87	2.51	2.45
S <sub>22</sub> (ohms)	3.66	3.68	3.48

Note: The values in the table above were calculated using equation 7 and the Q – factor values from table 5.

#### 4. CONCLUSION

#### 4.1 Q – Factor and Q – Ratio Analysis

To summarize, the trombone coil design was evaluated at three different physical lengths—12 cm (the minimum length), 13 cm (maximum length), and a medium-length when it was tuned to 123.20 MHz. The primary goal was to confirm an improvement in tuning efficiency and maintaining scanning accuracy while taking into account external, loading, and unknown variables.

Based on the Q-factor values presented in Table 3, a trend was observed: the Q-factor decreases as the coil is loaded due to energy loss from the body or phantom sample. Across all configurations, the unloaded Q-factors were significantly higher than their loaded counterparts, confirming that the sample dominates the energy loss which is desirable outcome for RF coil performance in MRI.

Furthermore, both  $S_{11}$  and  $S_{22}$ , the *Q-ratios* were consistently above 2.4, with the highest values recorded at the 12 cm length (up to 3.66) and when the coil was tuned at 123.20 MHz (up to 3.68). Since the Q-ratios were all greater than 1, this indicates that the coil losses were relatively low compared to sample losses, meaning the coil design performs efficiently across the tested configurations.

While all configurations demonstrated adequate performance, the medium-length coil (tuned to the exact Larmor frequency of 123.20 MHz) offered a strong balance between efficient energy transfer and minimized reflection, as reflected in the Q-ratios of 2.51 and 3.68. Since the

Q-ratio for the coil while resonating at 123.20 MHz was above 1, this indicates that for future invivo studies, the coil will maintain a high SNR.

# **4.2** Future Improvements

In the future, it would be beneficial to reconstruct the trombone coil in a way where there is more structural support around circuitry components such as the matching capacitors and baluns. Because these components had to be shielded along with the coil, there were some issues with broken signal lines when actively adjusting the length of the coil. In addition to adding structural support around the circuitry, making the bounding acrylic plates thicker would decrease the risk of the coil breaking during use. Overall, it takes a lot of force to increase and decrease the length of the coil, so increasing the durability of the coil would be a future priority.

The next step in benchtop testing would be to combine the ports of the coil to take measurements using the coil's quadrature ability. Traditionally, birdcage coils are able to have a strong homogenous field with little RF power loss due to their quadrature characteristic. In short, quadrature is the ability of a coil to have two perpendicular coils driven by a sinusoidal current that are 90 degrees out of phase from one another. In terms of the trombone coil, the two ports must be combined using a quad combiner which ultimately will combine perpendicular coils so that a reading can be taken using the coil in quadrature. Once the trombone coil is verified in quadrature, in vivo studies will be done to image mice and other small animals.

#### REFERENCES

- [1] H. H. Schild, "MRI made easy: (... well almost)," Berlin: Schering Ag, 1990.
- [2] L. M. M. D., M. S. Fayad, *CT Scan Versus MRI Versus X-Ray: What Type of Imaging Do I Need?*, Johns Hopkins Medicine., Accessed: Jan. 20, 2025. [Online]. Available: https://www.hopkinsmedicine.org/health/treatment-tests-and-therapies/ct-vs-mri-vs-xray
- [3] A. D. Elster, *Larmor frequency*, Questions and Answers in MRI., Accessed: Jan. 20, 2025. [Online]. Available: https://mriquestions.com/who-was-larmor.html#/
- [4] C. Westbrook, "MRI at a Glance," John Wiley & Sons, 2009.
- [5] H. Asano et al., Deuterium Magnetic Resonance Imaging Using Deuterated Water-Induced 2H-Tissue Labeling Allows Monitoring Cancer Treatment at Clinical Field Strength, Clinical Cancer Research, vol. 29, no. 24, pp. 5173–5182, 2023, doi: 10.1158/1078-0432.ccr-23-1635.
- [6] J. Mispelter, M. Lupu, and A. Briguet, "NMR Probeheads for Biophysical and Biomedical Experiments," IMPERIAL COLLEGE PRESS, 2011. doi: doi:10.1142/p759.
- [7] M. Brown and R. C. Semelka, "MRI," John Wiley & Sons, 2003. doi: 10.1002/0471467936.
- [8] P. Balchandani and T. P. Naidich, *Ultra-High-Field MR Neuroimaging*, American Journal of Neuroradiology, vol. 36, no. 7, pp. 1204–1215, 2015, doi: 10.3174/ajnr.A4180.
- [9] B. Vachha and S. Y. Huang, MRI with ultrahigh field strength and high-performance gradients: challenges and opportunities for clinical neuroimaging at 7 T and beyond, Eur Radiol Exp, vol. 5, no. 1, p. 35, 2021, doi: 10.1186/s41747-021-00216-2.

- [10] A. D. Elster, *Magnetic field strength*, Questions and Answers in MRI., Accessed: Jan. 21, 2025. [Online]. Available: https://mriquestions.com/how-strong-is-30t.html#/
- [11] A. S. Minhas and R. Oliver, "Magnetic Resonance Imaging Basics," Adv Exp Med Biol, vol. 1380, pp. 47–82, 2022, doi: 10.1007/978-3-031-03873-0 3/FIGURES/19.
- [12] B. Gruber, M. Froeling, T. Leiner, and D. W. J. Klomp, *RF coils: A practical guide for nonphysicists*, Journal of Magnetic Resonance Imaging, vol. 48, no. 3, pp. 590–604, 2018, doi: 10.1002/jmri.26187.
- [13] A. Prasad, *Make in India': lessons from G. Suryan's NMR research*, Curr Sci, vol. 110, no. 8, pp. 1402–1404, 2016, doi: 10.2307/24908091.
- [14] S. J. Holdsworth and R. Bammer, *Magnetic Resonance Imaging Techniques:* fMRI, DWI, and PWI, Semin Neurol, vol. 28, no. 4, pp. 395–406, 2008, doi: 10.1055/s-0028-1083697.
- [15] N. Gurler and Y. Ziya Ider, FEM based Design and Simulation Tool for MRI

  Birdcage Coils including Eigenfrequency Analysis, 2012. [Online]. Available:

  https://mriquestions.com/uploads/3/4/5/7/34572113/13978\_gurler\_paper\_birdcage
  \_design.pdf
- [16] C. E. Hayes, *The development of the birdcage resonator: A historical perspective*, John Wiley & Sons., 2009. doi: 10.1002/nbm.1431.
- [17] Y. Xu and P. Tang, Easy fabrication of a tunable high-pass birdcage resonator, Magn Reson Med, vol. 38, no. 1, pp. 168–172, 1997, doi: 10.1002/mrm.1910380123.
- [18] A. D. Elster, *Linear v Quadrature coils*, Questions and Answers in MRI., Accessed: Jan. 21, 2025. [Online]. Available: https://mriquestions.com/lp-vs-cp-quadrature.html#/
- [19] M. Mcdougall, D. Brown, D. Spence, and S. Wright, *A Low-Pass Trombone Birdcage Coil with Broad Tuning Range*, Proc. Intl. Soc. Mag. Reson. Med, vol. 9, p. 1092, 2001, [Online]. Available: https://cds.ismrm.org/ismrm-2001/PDF4/1092.pdf

- [20] C.-L. Chin, C. M. Collins, S. Li, B. J. Dardzinski, and M. S. Smith, BirdcageBuilder: Design of specified-geometry birdcage coils with desired current pattern and resonant frequency, vol. 15, no. 2, pp. 156–163, 2002, doi: 10.1002/cmr.10030.
- [21] M. Vít et al., *A broad tunable birdcage coil for mouse 1H/19F MR applications*, Journal of Magnetic Resonance, vol. 329, p. 107023, 2021, doi: 10.1016/j.jmr.2021.107023.

## **APPENDIX: A - LOGARITHMIC MAGNITUDE PLOTS**

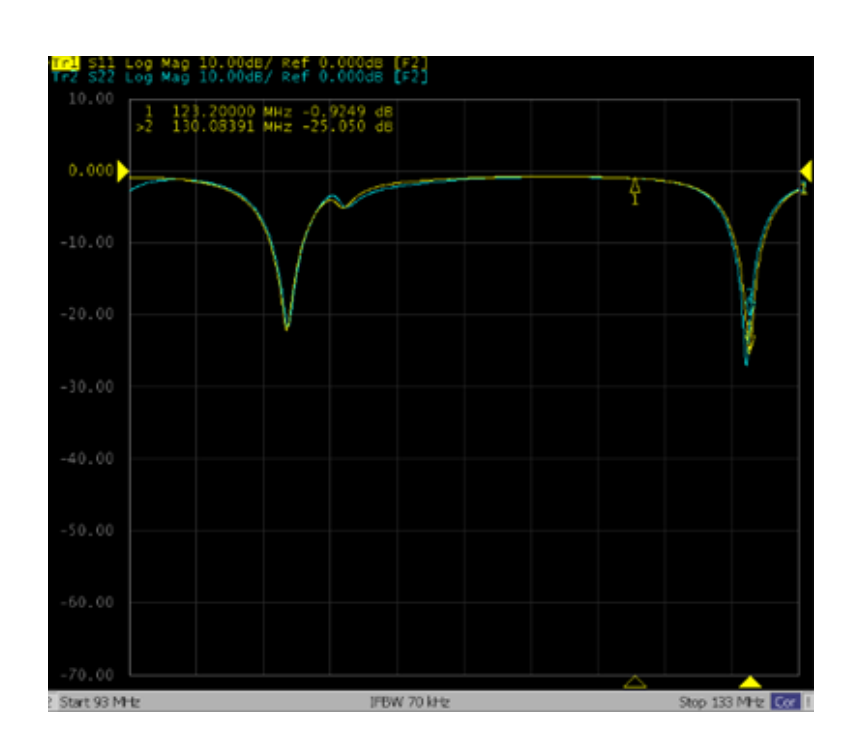


Figure A.1: Log Mag of S11 at 12 cm Coil Length Unloaded

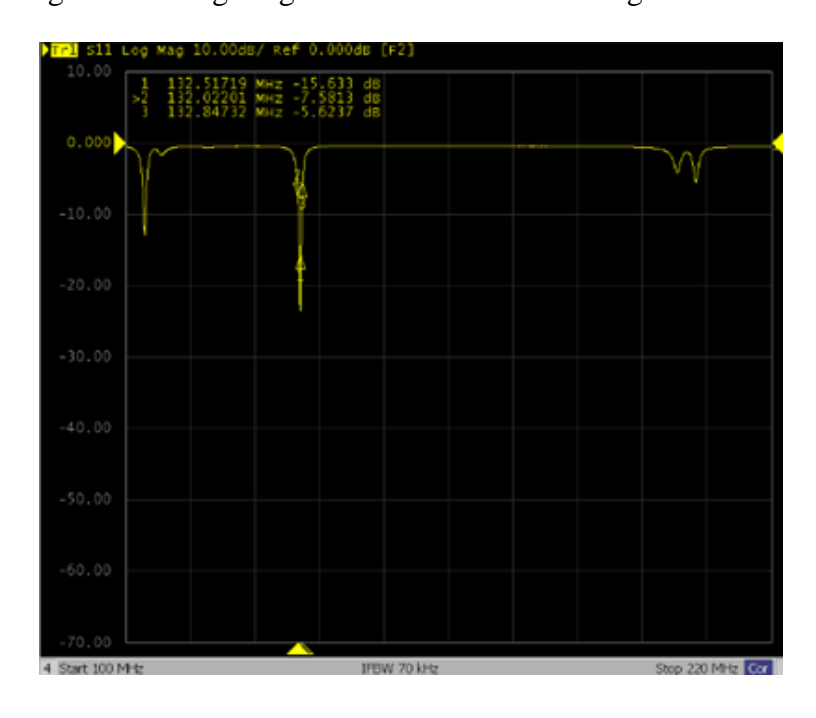


Figure A.2: Log Mag of S11 at 12 cm Coil Length Loaded

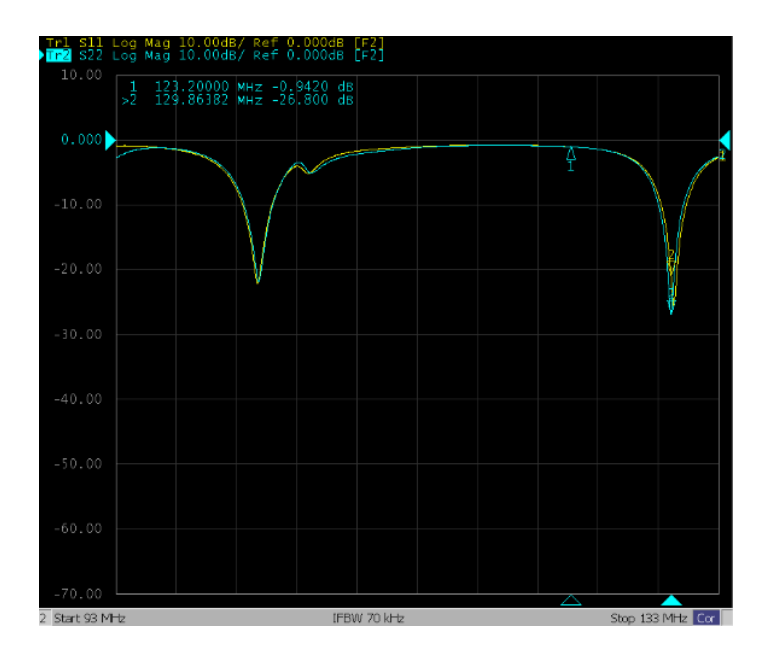


Figure A.3: Log Mag of S22 at 12 cm Coil Length Unloaded



Figure A.4: Log Mag of S22 at 12 cm Coil Length Loaded

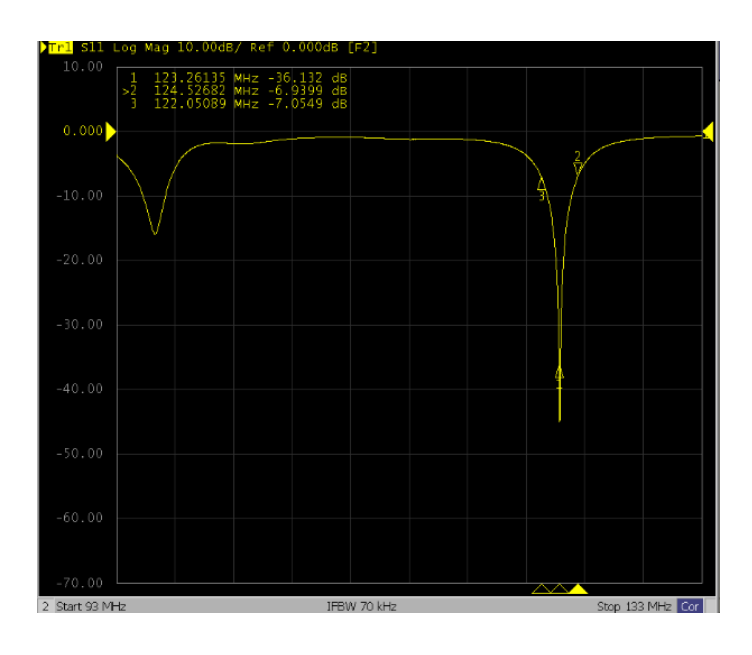


Figure A.5: Log Mag of S11 Tuned to 123.20 MHz Unloaded

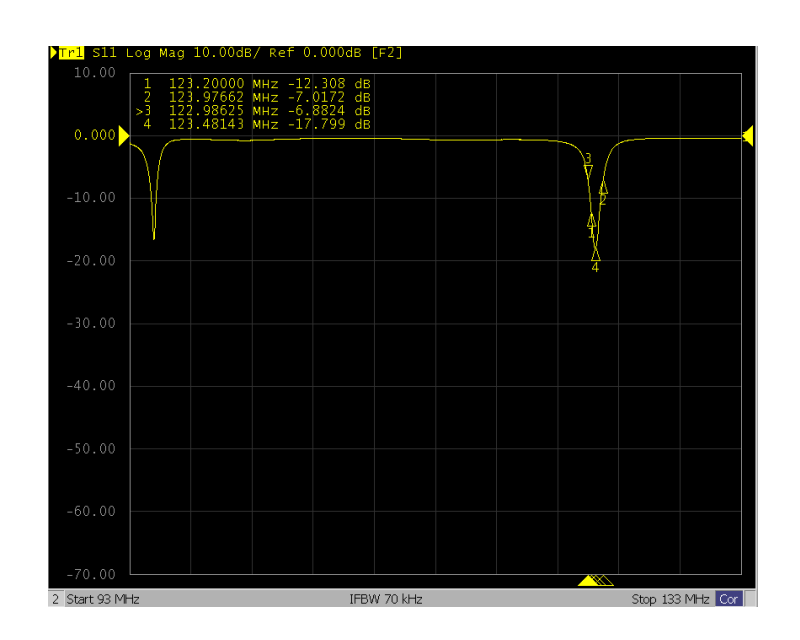


Figure A.6: Log Mag of S11 Tuned to 123.20 MHz Loaded

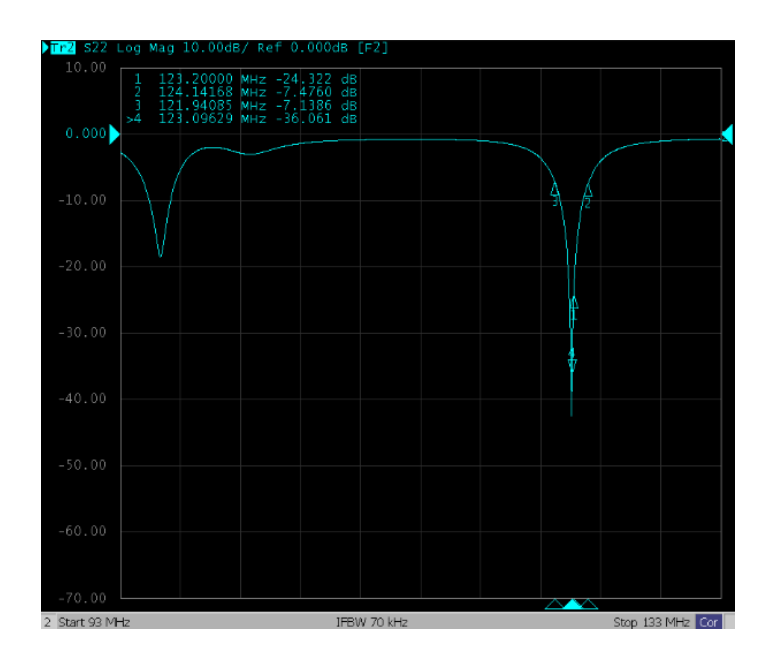


Figure A.7: Log Mag of S22 Tuned to 123.20 MHz Unloaded

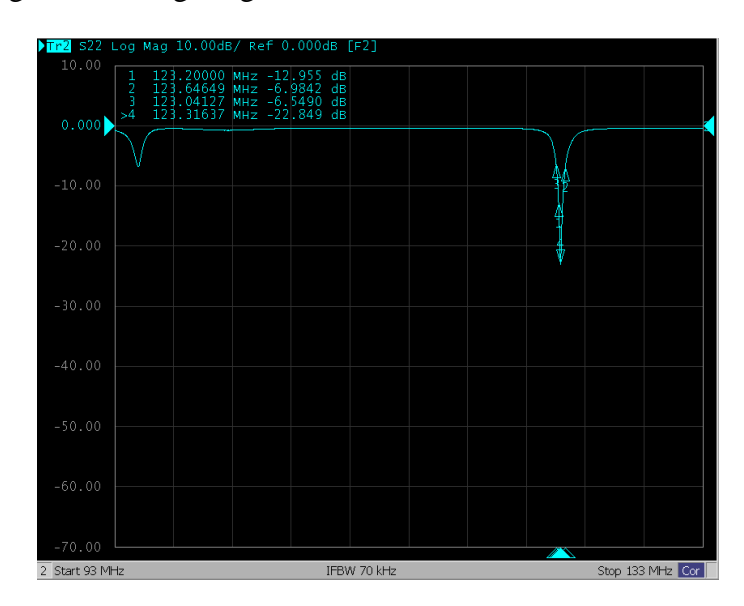


Figure A.8: Log Mag of S22 Tuned to 123.20 MHz Loaded

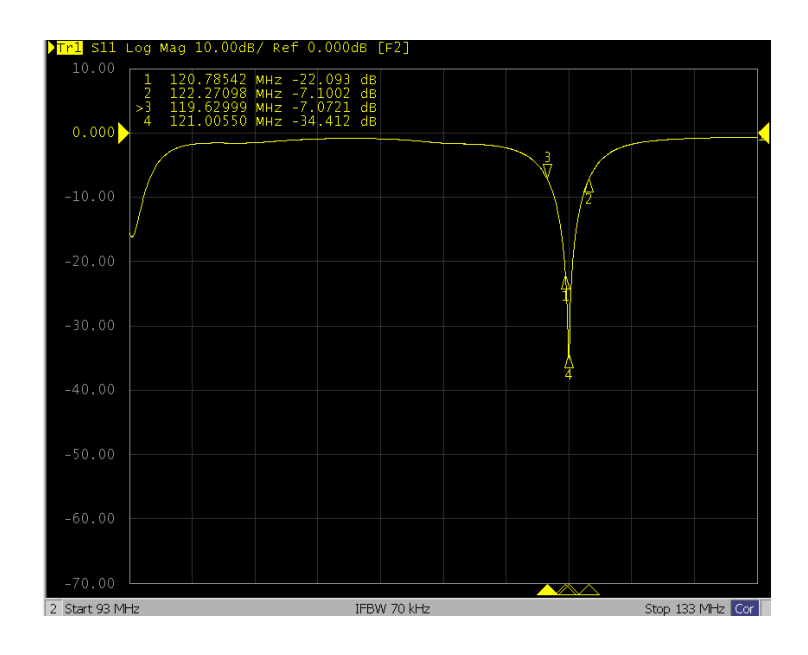


Figure A.9: Log Mag of S11 at 13 cm (maximum length) Coil Length Unloaded

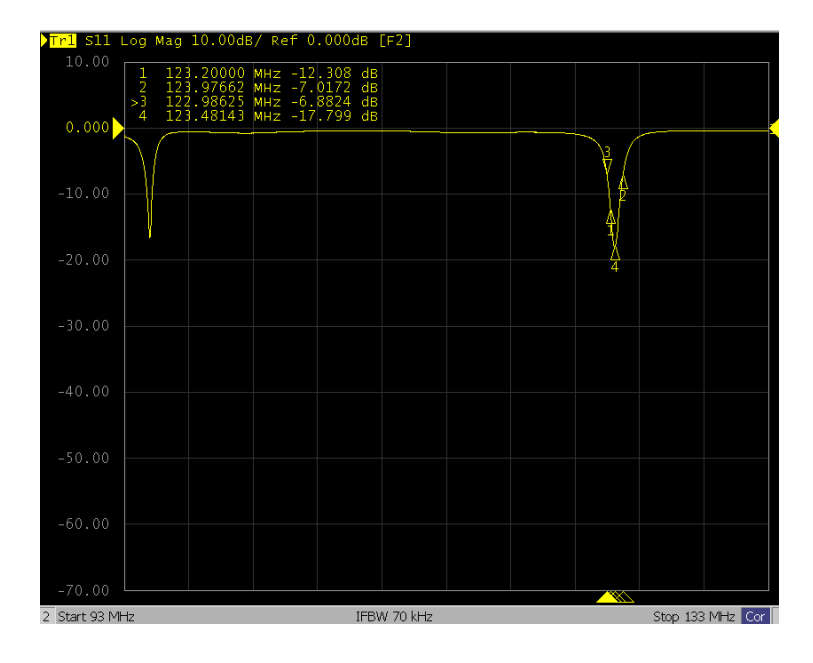


Figure A.10: Log Mag of S11 at 13 cm (maximum length) Coil Length Loaded

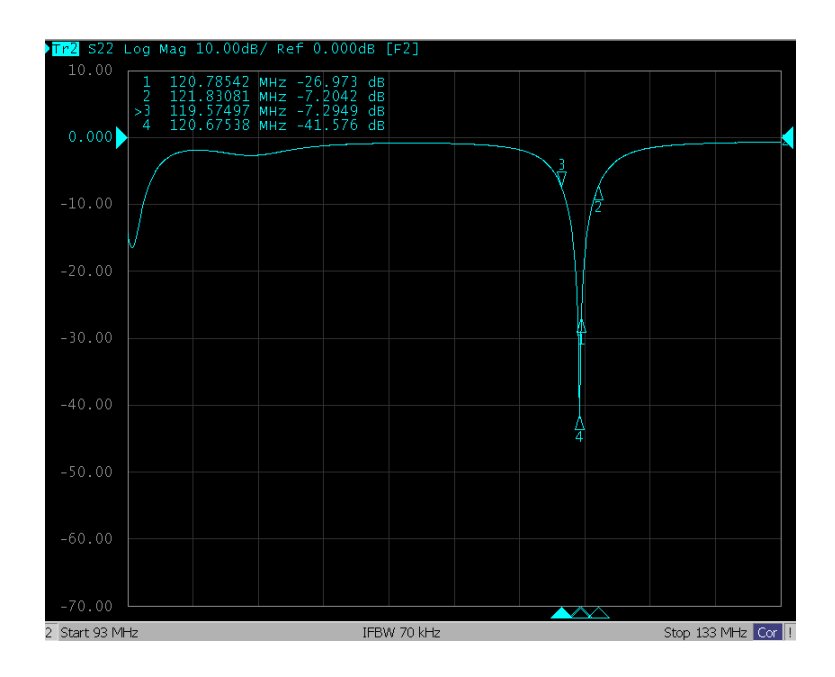


Figure A.11: Log Mag of S22 at 13 cm (maximum length) Coil Length Unloaded



Figure A.12: Log Mag of S22 at 13 cm (maximum length) Coil Length Loaded

## **APPENDIX: B – SMITH CHARTS**

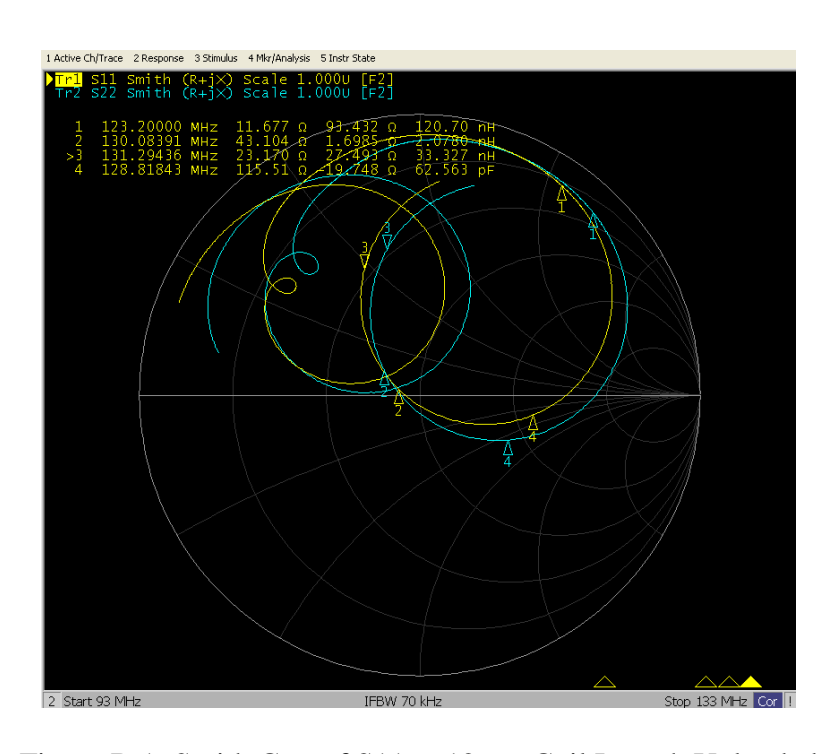


Figure B.1: Smith Cart of S11 at 12 cm Coil Length Unloaded

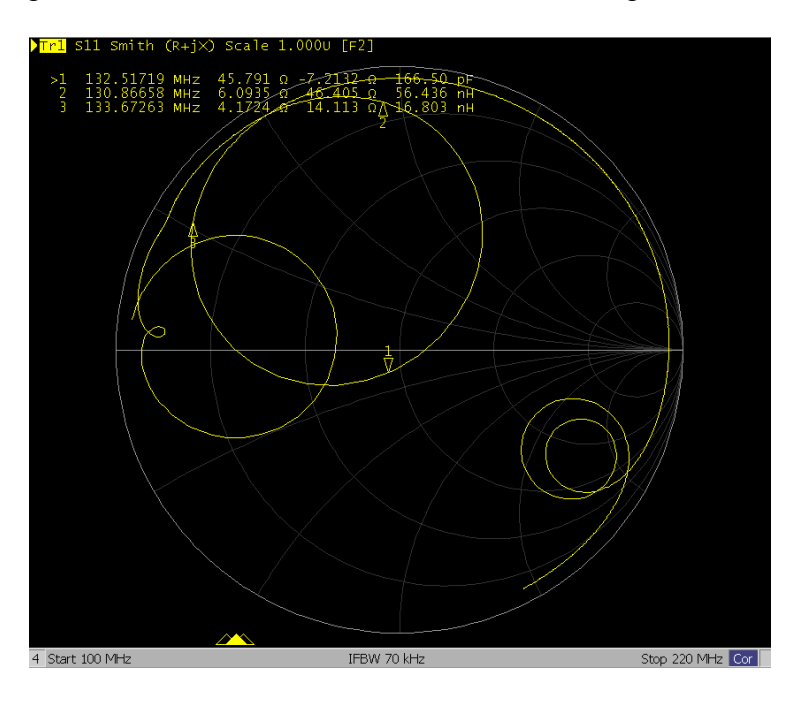


Figure B.2: Smith Cart of S11 at 12 cm Coil Length Loaded

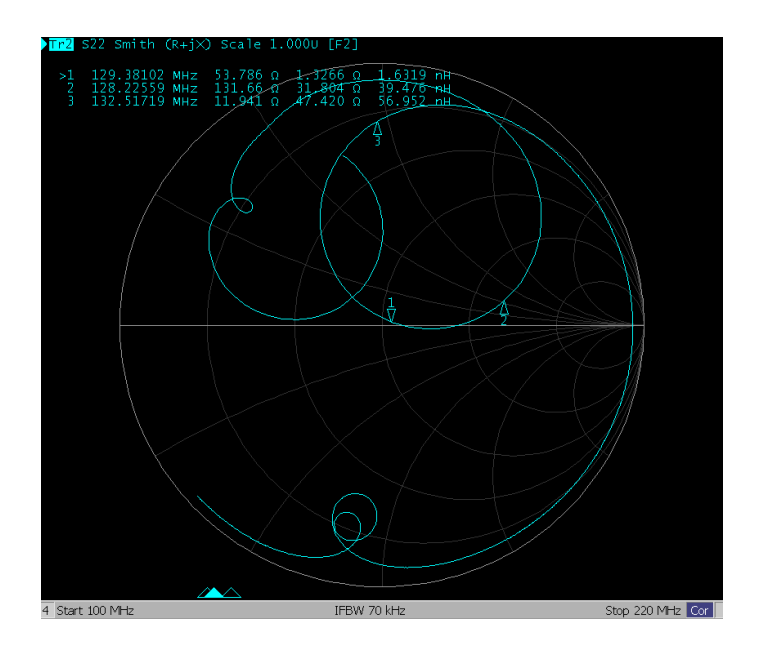


Figure B.3: Smith Cart of S22 at 12 cm Coil Length Unloaded

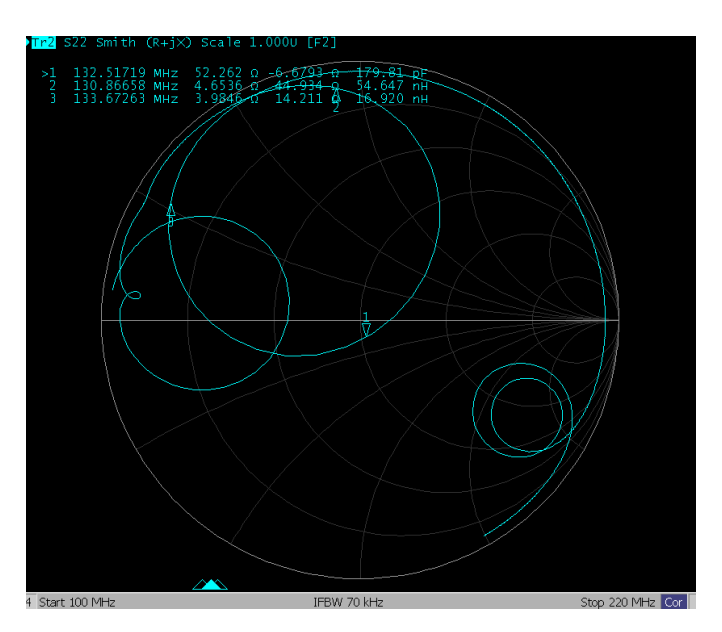


Figure B.4: Smith Cart of S22 at 12 cm Coil Length Loaded

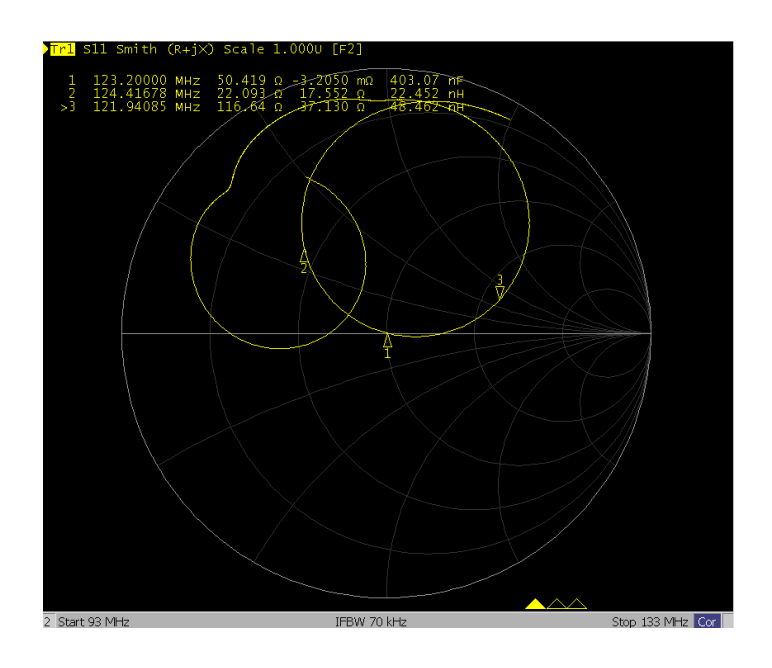


Figure B.5: Smith Cart of S11 Tuned to 123.20 MHz Unloaded

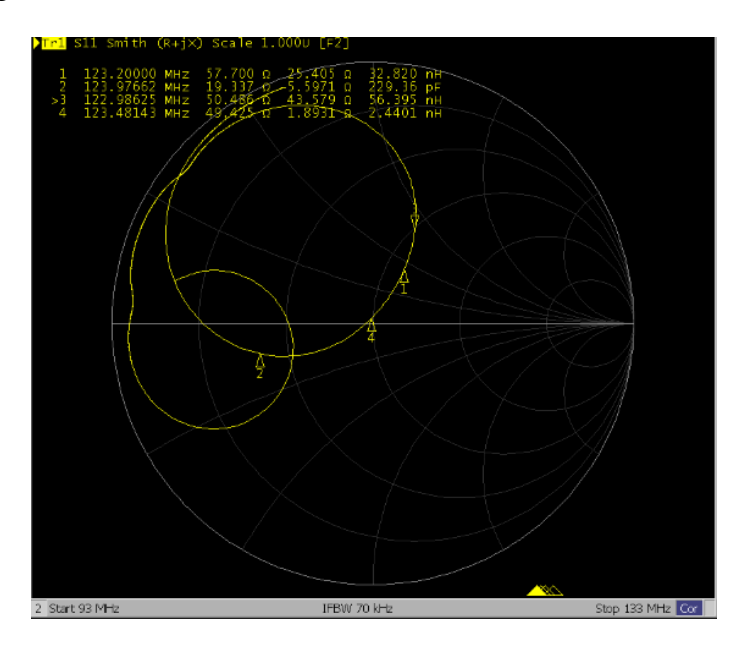


Figure B.6: Smith Cart of S11 Tuned to 123.20 MHz Loaded

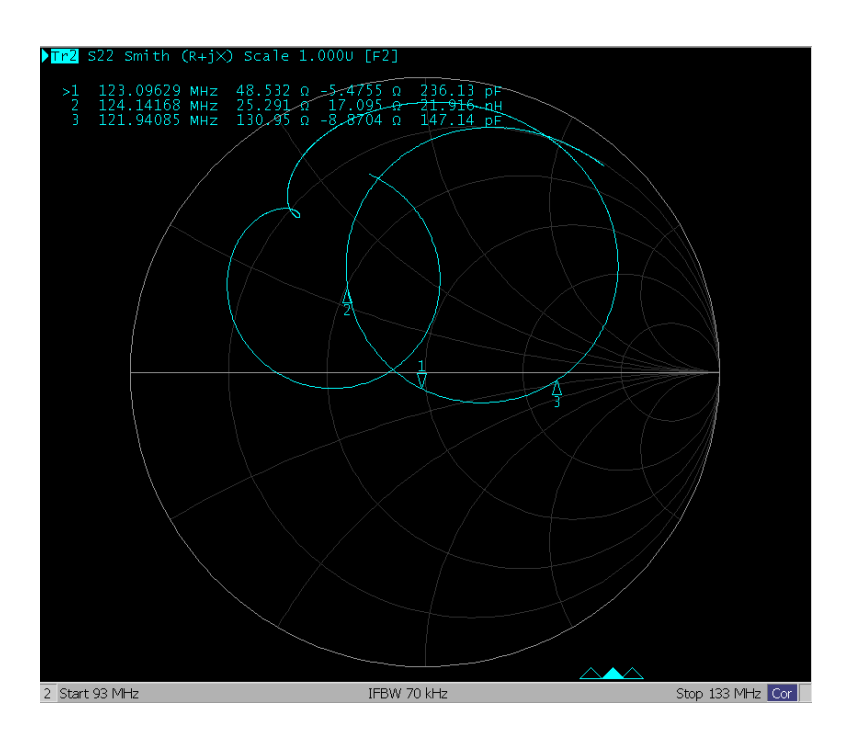


Figure B.7: Smith Cart of S22 Tuned to 123.20 MHz Unloaded

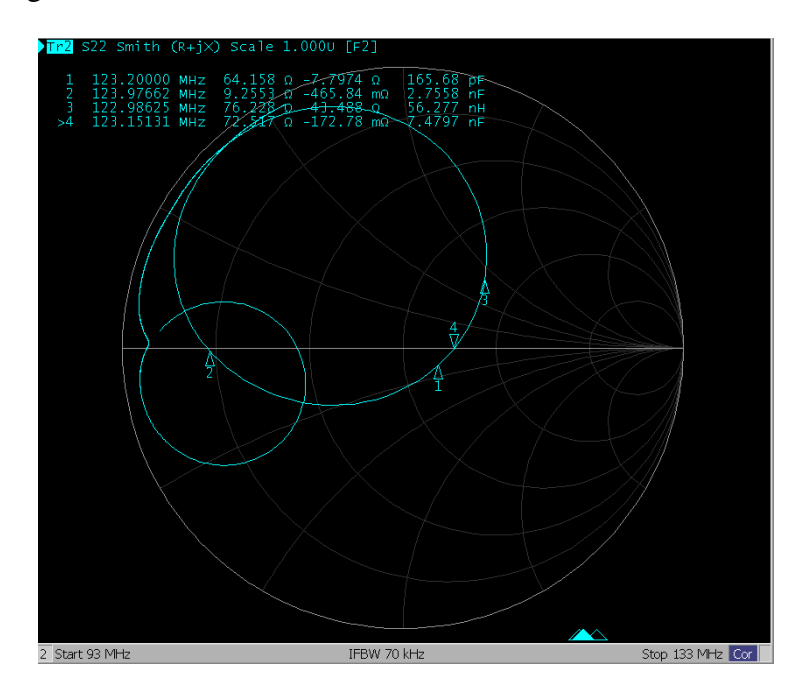


Figure B.8: Smith Cart of S22 Tuned to 123.20 MHz Loaded

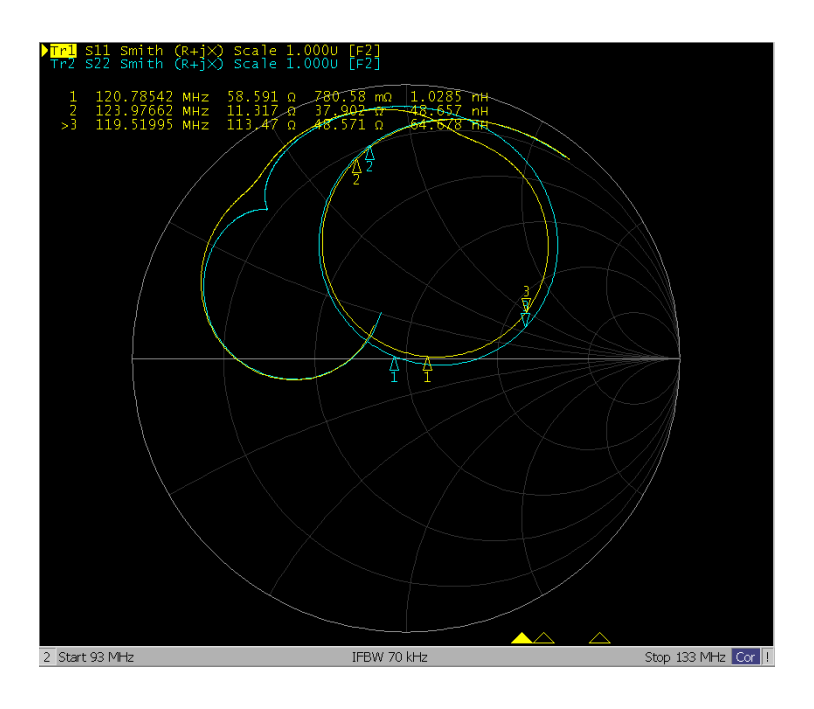


Figure B.9: Smith Cart of S11 13 cm (maximum length) Coil Length Unloaded

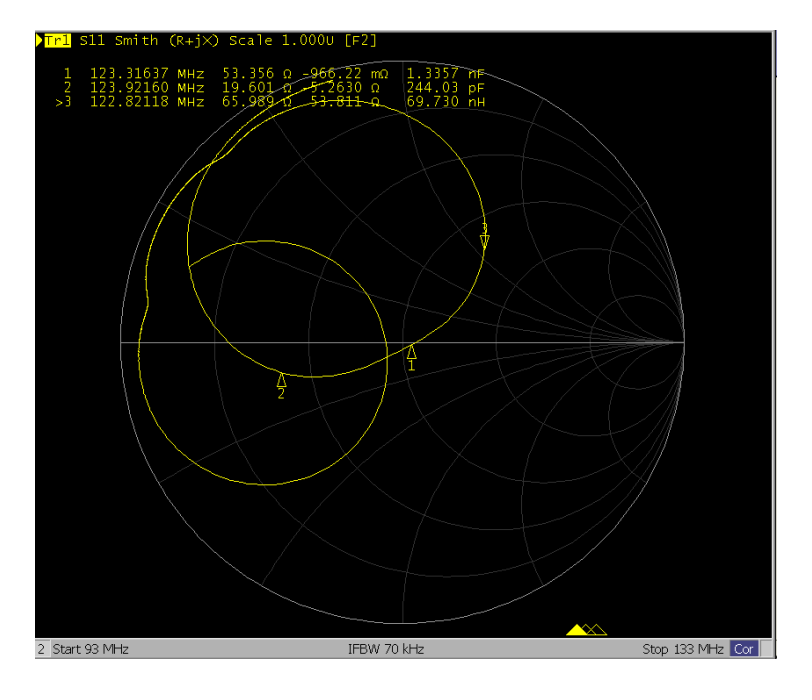


Figure B.10: Smith Cart of S11 13 cm (maximum length) Coil Length Loaded

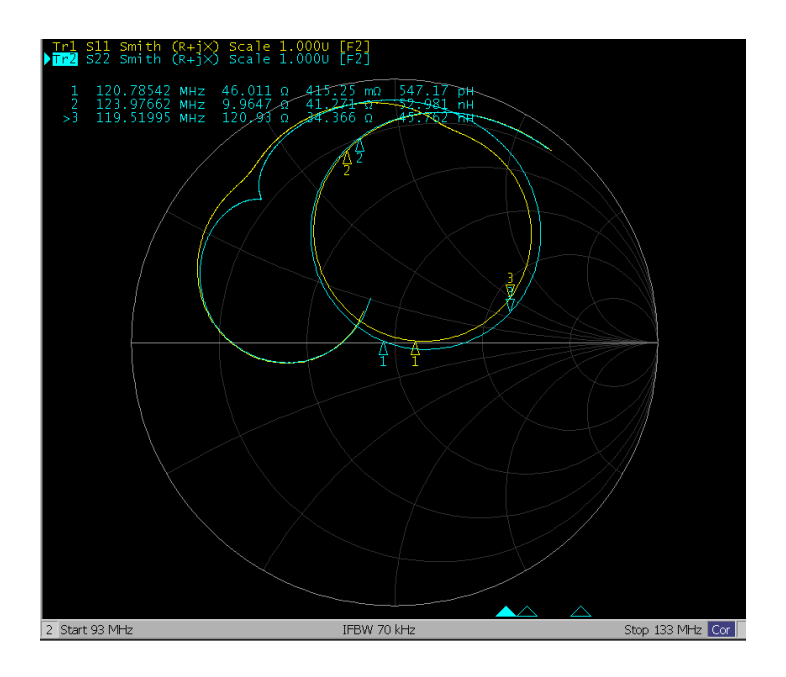


Figure B.11: Smith Cart of S22 13 cm (maximum length) Coil Length Unloaded

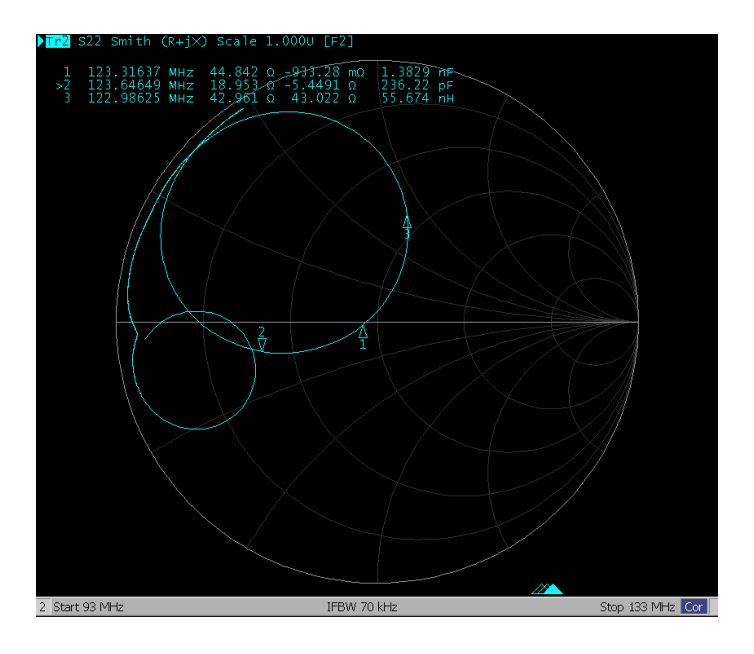


Figure B.12: Smith Cart of S22 13 cm (maximum length) Coil Length Loaded